The Astrophysical Journal, 736:16 (8pp), 2011 July 20 doi:10.1088/0004-637X/736/1/16
© 2011. The American Astronomical Society. All rights reserved. Printed in the U.S.A.

KINETIC CONDENSATION AND EVAPORATION OF METALLIC IRON AND IMPLICATIONS FOR METALLIC IRON DUST FORMATION

Shogo Tachibana, Hiroko Nagahara, Kazuhito Ozawa, Youhei Ikeda, Ryuichi Nomura, Keisuke Tatsumi, and Yui Joh
Department of Earth and Planetary Science, The University of Tokyo, 7-3-1 Hongo, Tokyo 113-0033, Japan; tachi@eps.s.u-tokyo.ac.jp
Received 2010 December 29; accepted 2011 April 27; published 2011 June 29

ABSTRACT

Metallic iron is one of the most abundant condensing materials in systems of solar abundance. Because metallic iron is responsible for the continuum opacity of dust particles, it has a large contribution to the thermal structure of circumstellar environments and hence to dust evolution itself. In order to understand the formation processes of metallic iron in circumstellar environments, condensation and evaporation kinetics of metallic iron were studied experimentally. Metallic iron condenses at the maximum rate with the condensation coefficient (a parameter ranging from 0 to 1 to represent kinetic hindrance for surface reaction) of unity under high supersaturation conditions, and evaporates nearly ideally (evaporation coefficient of unity) in vacuum. On the other hand, evaporation of metallic iron takes place with more kinetic hindrance in the presence of metallic iron vapor. It is also found that metallic iron atoms nucleate heterogeneously on Al_2O_3. Metallic iron does not necessarily condense homogeneously in circumstellar environments, but might condense through heterogeneous nucleation on pre-existing dust. Metallic iron formation proceeds with little kinetic hindrance for highly unequilibrated conditions, but the effects of kinetic hindrance may appear for evaporation and condensation occurring near equilibrium with a timescale of months to years in protoplanetary disks.

Key words: astrochemistry – meteorites, meteors, meteoroids – methods: laboratory – protoplanetary disks – stars: AGB and post-AGB

1. INTRODUCTION

Condensation and evaporation under non-equilibrium conditions are among the processes responsible for dust evolution in outflows of evolved stars and in protoplanetary disks. It is important to understand the kinetics of these processes for quantitative understanding of dust-forming conditions. Here we investigate the condensation and evaporation kinetics of metallic iron because (1) metallic iron is one of the most abundant condensing materials in systems of solar abundance. It is commonly present in solar system materials such as chondritic meteorites, interplanetary dust particles, and cometary particles. Its possible presence in oxygen-rich dust shells around evolved stars has also been proposed to explain the high near-infrared opacity of the shell (e.g., Kemper et al. 2002). (2) Metallic iron is an efficient absorber of light and responsible for the continuum opacity of dust particles. The interaction of metallic iron dust with the radiation field makes a large contribution to the thermal structure of circumstellar environments and hence to dust evolution itself.

The evaporation and/or condensation flux of metallic iron under low-pressure conditions is expressed by the kinetic theory of gases as a function of the partial pressure of metallic iron (p), the equilibrium vapor pressure of metallic iron ($p^{\rm eq}$), and temperature:

$$J = \frac{\alpha_c p - \alpha_e p^{\rm eq}}{\sqrt{2\pi m k T}}, \quad (1)$$

where m is the atomic weight of iron, k is the Boltzmann constant, T is the absolute temperature, and $\alpha_{\rm c}$ and $\alpha_{\rm e}$ are the condensation and evaporation coefficients, respectively, ranging from 0 to 1 to represent kinetic hindrances (Paule & Margrave 1967). Condensation and evaporation proceed without kinetic hindrances when $\alpha_{\rm c}$ and $\alpha_{\rm e}$ are equal to unity. Because these coefficients change the timescale of dust growth significantly, determination of these parameters is important to understand dust evolution.

Kinetic hindrances for condensation and evaporation are attributed to surface atomistic processes such as adsorption of gas, surface diffusion and desorption of adsorbed atoms, and formation and breaking of bonds. The surface atomistic structure such as the number of kink sites, which are energetically favored sites for atoms to break bonds or to be incorporated into a crystal lattice, also contributes to kinetic hindrances. It is hardly possible to determine the extent of kinetic hindrance theoretically, so that $\alpha_{\rm c}$ and $\alpha_{\rm e}$ should be determined experimentally as a function of temperature, pressure, and gas chemistry.

The evaporation coefficient for the free evaporation ($p = 0$) of metallic iron has been estimated to be close to unity (Tsuchiyama & Fujimoto 1995), which is larger than that for forsterite (0.1–0.01, depending on temperature and crystallographic orientation; e.g., Takigawa et al. 2009). However, there have been no data on $\alpha_{\rm e}$ for the evaporation of metallic iron in the presence of iron gas, which is a more realistic evaporation condition in circumstellar environments, especially in protoplanetary disks. The mean free path of gas species in protoplanetary disks with a total pressure of 10^{-5} atm (mainly H_2) is several centimeters at ~1400 K, and thus not only do the surrounding iron gas atoms have a chance of hitting the evaporating surface but evaporated iron atoms can also affect the kinetic hindrance for evaporation. Moreover, no $\alpha_{\rm c}$ has been reported for the condensation of metallic iron.

In this study, we carried out evaporation and condensation experiments for metallic iron under known pressure conditions of metallic iron vapor. We introduce our experimental methods in Section 2. We show results of experiments in Section 3, and discuss $\alpha_{\rm c}$ and $\alpha_{\rm e}$ and their dependence on temperature and $p/p^{\rm eq}$ in Section 4. We further discuss the implications of these measurements for dust evolution in circumstellar environments in Section 5, and summarize and conclude in Section 6.

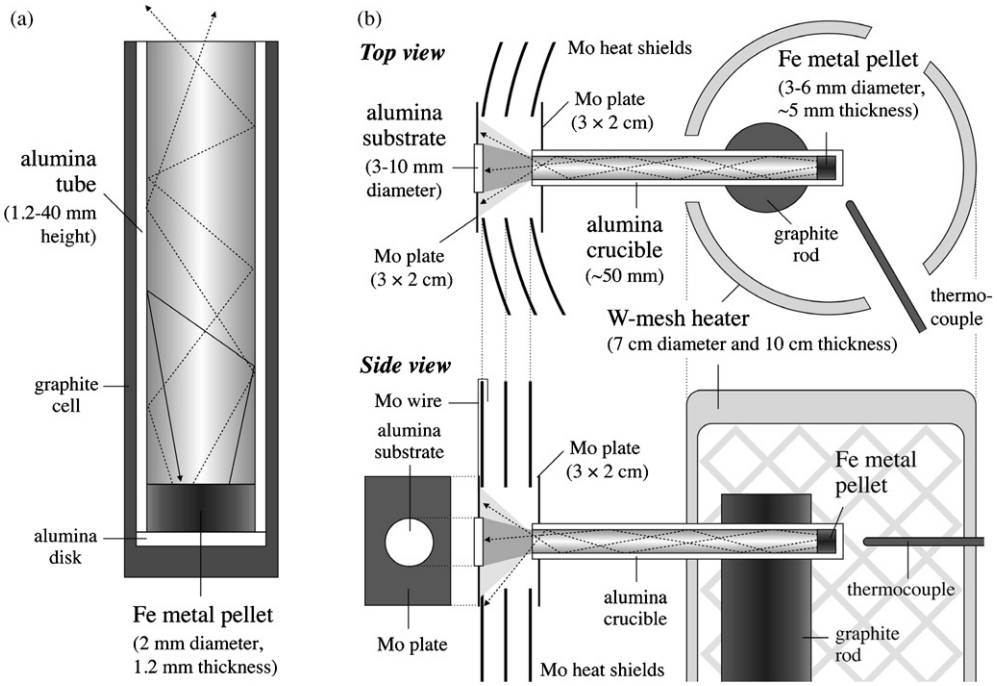

Figure 1. Schematic illustrations of experimental setups. (a) A cross section of an alumina tube with a metal pellet in one end used for the evaporation experiments of metallic iron in the presence of iron gas. (b) Top and side views of the furnace setup for the condensation experiments.

2. EXPERIMENTS

2.1. Evaporation of Metallic Iron in the Presence of Ambient Iron Gas

Pellets (2 mm in diameter and 1.2 mm in thickness) of metallic iron were put in the ends of a series of alumina tubes, the inner and outer diameters of which were 2 and 3 mm, respectively, and heights ranged from 1.2 to 40 mm. One end of the alumina tube, in which the pellet was put, was covered with an alumina disk, and the tube and disk were inserted into a graphite capsule (Figure 1(a)). The tubes were put in an isothermal region of a tungsten-mesh heater (5 cm in diameter and 10 cm in height), which was set in a vacuum chamber (22 cm diameter and 35 cm height) connected to a turbo molecular pump and a rotary pump (Ozawa & Nagahara 2000; Tachibana et al. 2002), and preheated at 770 K for a few hours to evacuate residual air and gases from furnace materials. The temperature of the furnace was then raised to a desired heating temperature (1720–1350 K), which was calibrated to within an uncertainty of ±5 K using the melting temperatures of Ag, Au, Cu, and Ni, and the eutectic temperature of Ni–C (1600 K), at the rate of ∼20 K minute^{-1}. The tubes were heated at the experimental temperatures for times ranging from 0.75 to 400 hr. Since the tubes have gas flow conductance, part of the evaporated iron gas always resides in the tubes and evaporation occurs in the presence of metallic iron gas (Figure 1(a)). After the desired duration of heating, the samples were quenched by shutting off the power supply. The pressure in the vacuum chamber, which was continuously evacuated during the experiments, was $\leqslant 10^{-3}$ Pa at higher experimental temperatures (>1550 K) or $\sim 10^{-5}$ Pa at lower temperatures (<1400 K). The evaporation rate of the pellet was evaluated from the weight loss of the iron pellet, which was measured by an electric microbalance to a precision of 0.01 mg.

2.2. Condensation of Metallic Iron Under Known Supersaturation Ratios

A metallic iron pellet (3–6 mm in diameter and ∼0.5 mm in thickness) was placed at the bottom of a ∼50 mm long alumina crucible, of which the inner diameter ranged from 3 to 6 mm depending on the size of the metallic iron pellet, and preheated at 770 K for a few hours by a tungsten-mesh heater (7 cm in diameter and 10 cm in height) in a vacuum chamber (25 cm diameter and 50 cm height). The temperature of the furnace was raised to a desired heating temperature (1510–1680 K) at a rate of ∼20 K minute^{-1} and heated for 3–90 hr in order to generate atomic iron gas from the metallic iron pellet (Figure 1(b)). A part of the gas that evaporated through the alumina tube impinged and condensed on an alumina disk (3–10 mm in diameter and ∼1 mm in thickness), which was fixed to a molybdenum plate (2 cm × 3 cm) and hung to the hole of multi-layer molybdenum heat shields (1 cm × 2 cm; Figure 1(b)). The outlet of the alumina tube with a molybdenum plate was placed close to the hole of the innermost heat shield in order to let evaporated iron gas atoms flow only through the hole of the heat shields and to avoid contamination from furnace materials. The distance between the substrate and the outlet of the tube was varied between 5 and 17.5 mm.

The substrate was heated by indirect radiation through the hole of layered heat shields, and its temperature was determined with an uncertainty of ±3 K by calibrating against the melting points of Ag and Au. The pressure in the chamber was kept below 10^{-3} Pa during experiments by continuous evacuation of the chamber with a turbo-molecular pump and a rotary pump. The mean free path of iron atoms that escaped from the tube should be much longer than the distance between the substrate and the outlet of the tube, and direct incoming gas atoms from the tube impinge onto the substrate without thermal accommodation by gas-phase collisions. The direct incoming

gas atoms thus have velocities representative of the temperature of the tube, which was almost isothermal in the inside of the tungsten-mesh heater but decreased toward the outlet of the tube. It should be noted however that the temperature of the outlet of the tube was higher than that of the substrate. Because such differences in the gas temperature may affect condensation behavior, condensation experiments at a substrate temperature of 1235 K were carried out for different incoming gas temperatures (1510, 1580, and 1639 K; the temperature of the iron pellet), where the substrate temperature was kept constant for different gas source temperatures by changing the position of the substrate in the furnace and the relative distance from the crucible.

The weight loss of the iron pellet and the weight gain of the alumina substrate were measured by an electric microbalance with a precision of 0.01 mg. The surface and cross section of the condensates were observed with a field-emission scanning electron microscope (FE-SEM), and the chemical composition and crystallinity of the condensates were analyzed with energy dispersive spectroscopy (EDS) and electron back-scattered diffraction (EBSD).

3. RESULTS

3.1. Evaporation Rate of Metallic Iron

The weight loss of the pellet increases linearly with time; the loss rate is larger in a shorter tube than in a longer tube because a longer tube has much more resistance to the gaseous flow, resulting in a higher iron vapor pressure near the surface of the pellet. We assume that evaporation takes place mostly from the upper surface of the pellet that evaporation from the side and bottom of the pellet is negligibly small and that the vapor pressure just above the upper surface of the pellet affects the evaporation rate. This assumption seems to be valid because the pellet was tightly fitted to the tube even after evaporation of a few tens of percent and step structures that formed by evaporation were observed only on the upper surface of the pellet. Moreover, even if there was a narrow gap between the pellet and the alumina crucible, evaporation from the gap may have been suppressed due to a high local vapor pressure of iron within the gap that should have high conductance for gas flow.

The vapor pressure near the sample surface is estimated from the weight loss of the pellet per unit time (dW/dt), the areas of the tube outlet (A), and the conductance of the tube (C; Paule & Margrave 1967):

$$p = \frac{dW/dt}{A}\left(\frac{1}{C} - 1\right)\sqrt{2\pi kT/m}, \quad (2)$$

where m is the atomic weight of iron, k is the Boltzmann constant, and T is the absolute temperature. The evaporation flux ($J_{\rm evap}$) for different lengths of tubes at temperatures ranging from 1718 to 1347 K are plotted as $J_{\rm evap}/J^{\rm id}_{\rm evap}$ against the undersaturation ratio (S) of $p/p^{\rm eq}$ in Figure 2, where $J^{\rm id}_{\rm evap}$ represents the ideal free evaporation rate ($p = 0$ and $\alpha_{\rm e} = 1$). The measured evaporation rate decreases as S increases due to recondensation from the surrounding gas. Experiments at the same temperature (1548 or 1448 K) with different heating durations show consistent results, which indicate that a steady ambient gas pressure condition was achieved and thus the evaporation rates were constant irrespective of heating duration. It should be noted that the evaporated fraction during heating to the experimental temperature and cooling to the room temperature was estimated to be at most a few percent for the experiments with the shortest duration (0.75 hr at 1720 K) and negligibly small in other cases.

3.2. Condensates and Condensation Rate of Metallic Iron

Energy dispersive spectroscopy and EBSD analyses showed that all the condensates are α-Fe, which may have been transformed from γ-Fe (the stable phase at substrate temperatures) during quench. Alternatively, the condensate might have been α-Fe even during its growth due to Ostwald's step rule, which states that the less stable form is more likely to nucleate from the vapor under the conditions where nucleation occurs. The latter possibility seems to be less likely because the condensed α-Fe would be transformed into γ-Fe at experimental temperatures.

Characteristic structures observed on the surface of condensates were growth steps with an interval of $\sim$10 nm (Figure 3(a)). Observation of condensates shows that metallic iron nucleates sporadically on the surface of corundum and eventually covers the entire surface, after which metallic iron grows on a compact metallic iron layer (Figure 3(b)).

The weight of the condensate increases linearly with time, and the weight loss of the gas source also has a linear dependence on time (Figure 4). This suggests steady condensation of metallic iron under conditions of constant supersaturation. The weight gains of the substrates were always smaller than the weight losses of the gas source, and $\sim$10%–30% of evaporated iron was condensed on the substrate depending on the distance between the outlet of the alumina tube and the substrate: the longer the distance, the smaller the recovered fraction. This is because only a certain fraction of evaporated iron atoms impinge on the surface of the substrate under the low-pressure molecular flow conditions and the incoming flux onto the substrate becomes smaller with increasing distance due to geometric reasons (Figure 1(b)).

Growth rates under different temperatures and supersaturation ratios were calculated from the steady weight gain of the substrate, the surface of which was covered by a compact metallic iron layer in order to eliminate the effect of heterogeneous nucleation of metallic iron onto the corundum substrate and the subsequent growth of heterogeneously nucleated metallic iron patches.

4. DISCUSSION

4.1. Evaporation Kinetics of Metallic Iron

The evaporation coefficient for free evaporation ($p/p^{\rm eq} = 0$) ($\alpha_{\rm e}(0)$) is obtained as the ratio between the experimental evaporation rate and the ideal evaporation rate given by Equation (1) with $\alpha_{\rm e} = 1$ and $p = 0$. The obtained $\alpha_{\rm e}(0)$ ranges from 0.9 at higher temperatures to 0.6 at lower temperatures, and its temperature dependence is expressed by

$$\ln \alpha_e(0) = 1.44(\pm 0.22) - 2595(\pm 353)/T. \quad (3)$$

The $\alpha_{\rm e}(0)$ in this study is consistent with that in Tsuchiyama & Fujimoto (1995), but shows a clearer dependence on temperature than in the previous study. The discrepancy may be due to the slight oxidation of metallic iron observed in Tsuchiyama & Fujimoto (1995) that may have affected evaporation. An interesting feature of the obtained temperature dependence is that $\alpha_{\rm e}(0)$ becomes unity at a temperature close to the melting point of metallic iron (1808 K). Similar temperature dependences of $\alpha_{\rm e}(0)$ have been reported for refractory oxides such as MgO, Al_2O_3, and Cr_2O_3 (Sata et al. 1978).

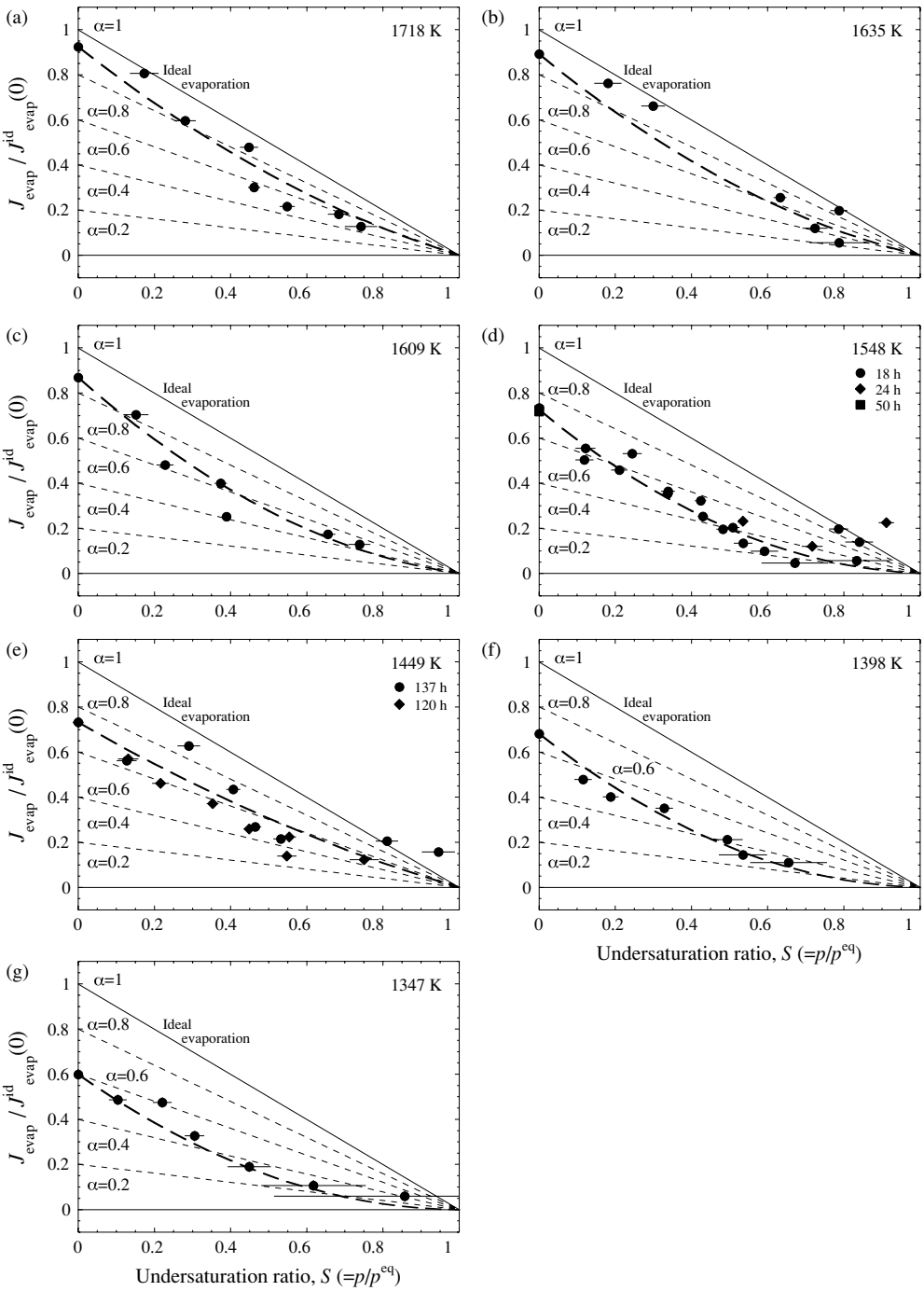

Figure 2. Evaporation flux (J_{evap}) of metallic iron, normalized to the ideal evaporation rate ($J^{id}_{evap}(0)$) in vacuum, plotted against the calculated undersaturation ratio, S (=p/p^{eq}). The ideal evaporation flux in the presence of iron vapor ($\alpha_e = \alpha_c = 1$) is shown as a thin solid line, and the fluxes with different values of α_e (α_c) are also shown (thin dashed lines). The thick dotted curve represents a quadratic fit to the experimental data (see the text for detail): (a) 1718 K, (b) 1635 K, (c) 1609 K, (d) 1548 K, (e) 1449 K, (f) 1398 K, and (g) 1347 K.

The relationship between the evaporation rate and the ambient iron gas pressure is not linear but convex (Figure 2). The evaporation rate should decrease linearly with p (Equation (1)) if α_e and α_c are equal to each other and constant irrespective of p, but this is not the case in the present study. This suggests that α_e and α_c both depend on the pressure of iron vapor. In order to clarify the pressure dependence of α_e and α_c, it is assumed that α_e and α_c are equal to each other and that they have linear dependence on the undersaturation ratio ($\alpha_e = \alpha_c = \alpha_e(0) + k\ (p/p^{eq})$), which yields a quadratic equation for the evaporation flux as a function of S. The evaporation rates at each temperature are fitted by a least-square technique, and the estimated k are -0.41 ± 0.12 (1σ) at 1718 K, -0.49 ± 0.18 at 1635 K, -0.63 ± 0.12 at 1609 K, -0.66 ± 0.08 at 1548 K, -0.24 ± 0.12 at 1449 K, -0.60 ± 0.05 at 1398 K, and -0.46 ± 0.09 at 1347 K. The negative values of k for all temperatures indicate that the kinetic barriers for evaporation and condensation at undersaturated conditions become larger at higher ambient gas pressure. Metal preferentially evaporates from kinks on the surface because it is easier energetically for

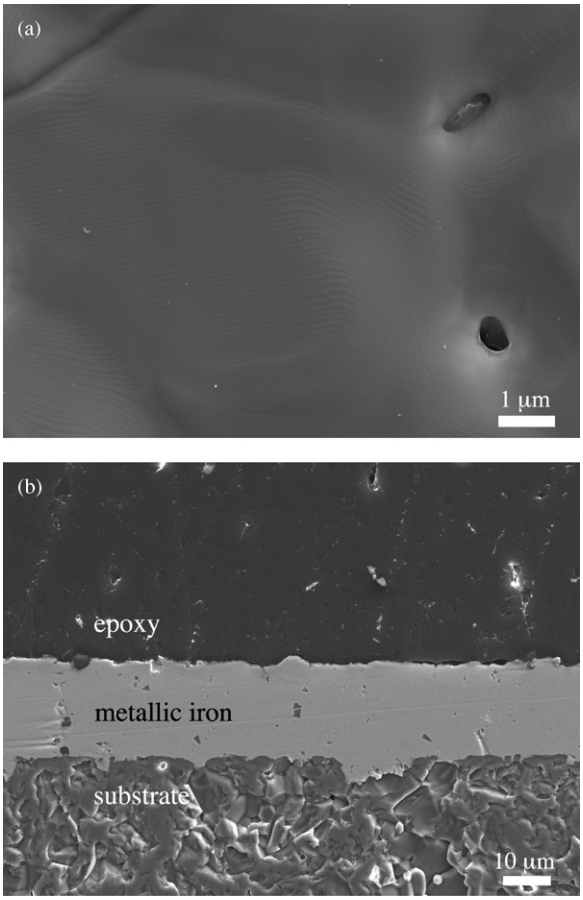

Figure 3. Secondary electron images of the surface (a) and the cross section (b) of metallic iron condensed at 1235 K for 48 hr.

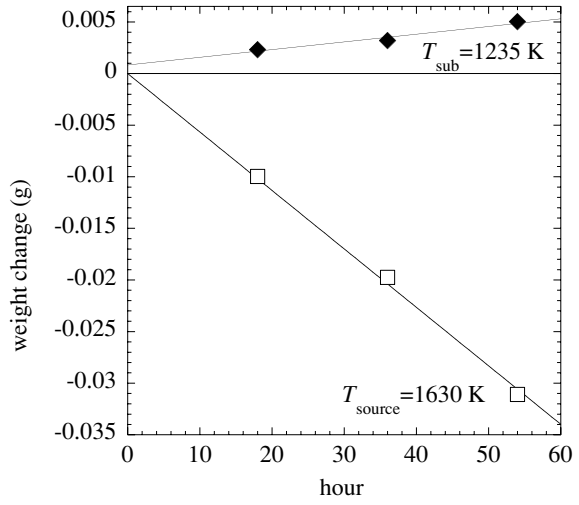

Figure 4. Weight loss of metallic iron (gas source) due to evaporation at 1630 K and the weight gain of the alumina substrate (1235 K) due to the condensation of metallic iron. The steady weight changes of the source and the substrate yield the incoming flux of iron onto the substrate and the condensation flux of metallic iron on the substrate, respectively.

atoms to break bonds with adjacent atoms, and condensation of incident metal atoms is also easier on a surface with many kink sites. The surface roughness (number of kinks), which thus affects the kinetic hindrances for evaporation and condensation, may be reduced near equilibrium, where the number of atoms breaking bonds at kink sites is balanced by the number of

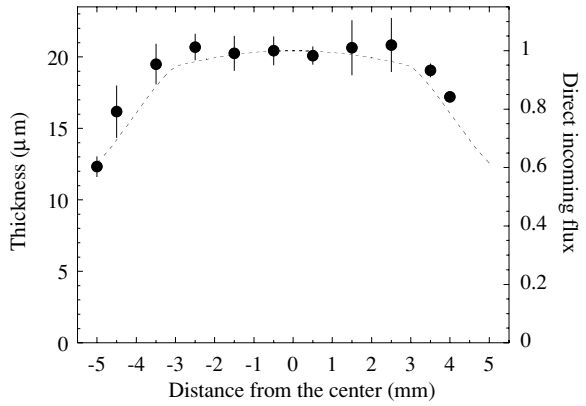

Figure 5. Thickness of condensed metallic iron (1235 K for 48 hr), shown in Figure 3, plotted against the distance from the center of the substrate (solid circles). Error bars represent the standard deviations of the means. The spatial variation of the direct incoming flux onto the substrate predicted by the flux distribution of vapor emerging from the tube (5.9 mm in diameter; Dayton 1956), which is normalized to the flux at the center of the substrate, is also shown (dashed curve).

atoms being incorporated into the crystalline lattice, as long as the temperature of the surface is lower than the thermal roughening temperature. The kinetic hindrance for condensation is therefore expected to be larger near equilibrium than under lower saturation conditions.

k seems to have a weak temperature dependence; however, the mean value of k is -0.54 ± 0.15 (1σ). Thus, α_e and α_c at undersaturation ($0 \leqslant S < 1$) can empirically be expressed by

$$\alpha_e = \alpha_c = \exp(1.44 - 2595/T) - 0.54(p/p^{eq})(p/p^{eq} < 1) \quad (4)$$

over the temperature range from 1720 to 1350 K. The evaporation rates calculated using Equation (4) are also shown in Figure 2.

4.2. Condensation Kinetics of Metallic Iron

A supersaturation ratio $S\,(p/p^{eq})$ at the surface of the substrate was calculated based on the direct incoming flux of iron onto the substrate that could be estimated from the flux distribution of vapor emerging from the tube under molecular flow conditions (Dayton 1956) and the measured evaporation rate of the iron gas source. The fraction of the flux onto the substrate relative to the total evaporation flux of metallic iron from the tube was calculated to range from 0.11 to 0.34 depending on the distance between the substrate and the outlet of the tube. Note that the usage of the tube has the effect of focusing gas flux from the tube outlet (Dayton 1956) and that the estimated fraction of the flux onto the substrate against the total evaporation flux here is much larger than that in the case without the tube.

There might have been other indirect fluxes of iron onto the substrate, which hit the substrate after colliding with the heat shields, and if they were present, the incoming flux onto the substrate would be underestimated. However, the thickness variation of the condensed metallic iron layer agrees well with the predicted spatial variation of direct flux onto the substrate (Figure 5), suggesting that the incoming flux of iron was dominated by the direct flux from the outlet of the tube because the indirect iron gas flux would come from random directions and its spatial variation would be uniform. We also found that condensation of metallic iron occurred on the molybdenum plate used to hold the Al_2O_3 substrate and on the heat shields at the

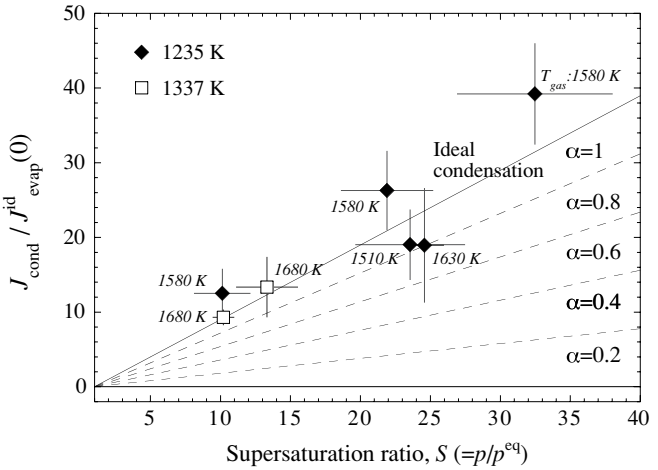

Figure 6. Condensation flux (J_{cond}) of metallic iron, normalized to the ideal evaporation rate ($J^{id}_{evap}(0)$) in vacuum, plotted against the supersaturation ratio, S (p/p^{eq}). Solid diamonds and open squares are the fluxes obtained at the substrate temperatures of 1235 and 1337 K, respectively. Temperatures shown with symbols (T_{gas}) represent those of gas-source metallic iron pellets (i.e., temperatures of the iron vapor colliding with the substrate). The ideal condensation flux ($\alpha_c = \alpha_e = 1$) is shown as a solid line, and the fluxes with different values of α_c (α_e) are also shown (dashed lines).

edge of the hole. The temperature of the heat shields should have been lower than that of the substrate because only the edge of the hole was heated by radiation, while the shield was cooled by thermal conduction to the interior. Therefore, the edge of the heat shields may not have acted as a reflector of impinging iron atoms but as a sink for them. This evidence suggests that the indirect iron gas flux onto the substrate was negligibly small, and thus further discussion will be made based on the estimate of the direct incoming flux.

The calculated direct incoming fluxes onto the substrate yield supersaturation ratios ranging from ~10 to ~35 in the present experiments. The condensation flux of metallic iron normalized to the ideal evaporation flux is shown as a function of S in Figure 6. Although the data are scattered to some extent, all of the measured condensation fluxes are close to the ideal value. This indicates that α_c is close to unity irrespective of α_e, because the effect of re-evaporation from the condensates must be small due to the large values of S. It is also seen that α_c at 1235 K does not depend on the temperature of incoming gas atoms, implying instantaneous thermal accommodation of the colliding gas atoms with the substrate surface.

The ideal condensation behavior of metallic iron in this study suggests that the condensation rate of metallic iron is determined by the supply of atomic iron gas and that surface atomistic processes are not the rate-limiting process at $S > 10$, i.e., the surface of the condensate is rough enough for all of the adsorbed atoms to find kink sites to be incorporated into the crystal lattice within their lifetime on the surface.

5. IMPLICATIONS FOR THE FORMATION OF METALLIC IRON IN CIRCUMSTELLAR ENVIRONMENTS

Homogeneous nucleation (nucleation without the aid of a substrate) and growth of metallic iron in a cooling gas have been discussed with the assumption that $\alpha_e = \alpha_c = 1$ (e.g., Blander & Katz 1967; Kozasa & Hasegawa 1987), and it has been concluded that the formation of metallic iron is significantly delayed due to a nucleation barrier caused by the large surface tension of iron. The present experiments show that metallic iron condenses at the maximum possible rate ($\alpha_c = 1$) under high supersaturation conditions ($S > 10$), and evaporates under nearly ideal conditions ($\alpha_e \sim 1$) at $S \sim 0$. These observations are consistent with the assumptions made in previous studies. However, we also show that the evaporation of metallic iron occurs with more kinetic hindrances at S close to 1, and that metallic iron nucleates heterogeneously on an Al_2O_3 substrate at $S > 10$. These effects were not included in previous models, so that we will now discuss the influences of heterogeneous nucleation and growth with kinetic hindrances on the formation of metallic iron in circumstellar environments.

We modeled metallic iron condensation on pre-existing corundum grains in two closed systems of the solar composition (Anders & Grevesse 1989) that cool isobarically at total pressures of 10^{-5} and 10^{-10} atm. These are conditions similar to those formed in protoplanetary disks and outflows from evolved stars, respectively. It was assumed that all aluminum atoms condensed as corundum spherules with a fixed uniform size (d_{cor}) that remained suspended in the gas until the nucleation of metallic iron. The size of the corundum grains changes depending on the cooling rate of the gas according to the homogeneous nucleation theory (e.g., Kozasa & Hasegawa 1987), but the condensation coefficient for homogeneous nucleation of corundum has not yet been determined. We therefore assume a fixed size for corundum condensates. The cooling timescale of τ_{cool} was given as $|d\ln T/dt|^{-1}$, which is the time required for the temperature to decrease by $1/e$.

Because the number of corundum condensates in the system and the surface area of each corundum grain are proportional to $1/d^3_{cor}$ and d^2_{cor}, the total surface area of the corundum grains is proportional to $1/d_{cor}$. The timescale for condensation is proportional to the total surface area of nucleation seeds (corundum grains in this case), and thus the condensation of metallic iron via heterogeneous nucleation on pre-existing solids proceeds in the same manner as long as τ_{cool}/d_{cor} is the same. For further discussion, we assume $d_{cor} = 1\,\mu$m because 1 μm sized corundum grains are commonly found in the acid residues of chondrites as solar and presolar grains (Nittler et al. 1997; Choi et al. 1998; Takigawa et al. 2011). We introduce a new cooling timescale of $\tau' = \tau_{cool}/(d_{cor}/1\,\mu\text{m})$, which ranged from 10^5 to 10^{12} s in the model.

The S required for heterogeneous nucleation (S_{crit}) was set to $S_{crit} = 10$ based on the present results. The condensation flux of iron was obtained using Equation (1) with the assumption that $\alpha_c = \alpha_e$, and α_c (α_e) was given by

$$\alpha_c = \alpha_e = 0.06 + \frac{0.94}{9}(p/p^{eq} - 1) \quad (1 \leqslant S \leqslant 10)$$
$$\alpha_c = \alpha_e = 1 \quad (S > 10), \tag{5}$$

which satisfied α_e in Equation (4) at 1347 K and $S = 1$ and α_c of unity at $S \geqslant 10$ (case (1)). No temperature dependence was assumed. Note that S_{crit} and the expression for α_c are not firmly defined and should be determined in further experimental studies. We also modeled the case of $\alpha_c = 1$ for comparison (case (2)).

Figure 7(a) summarizes the heterogeneous nucleation and condensation of metallic iron at a total pressure of 10^{-5} atm under different cooling conditions. The S_{crit} of 10 corresponds to supercooling to 75 K, which is smaller than values for S required for homogeneous nucleation (200–450 K). Hence, the nucleation delay of metallic iron is less significant than previously predicted, and metallic iron condenses more easily as long as pre-existing condensates act as nucleation seeds.

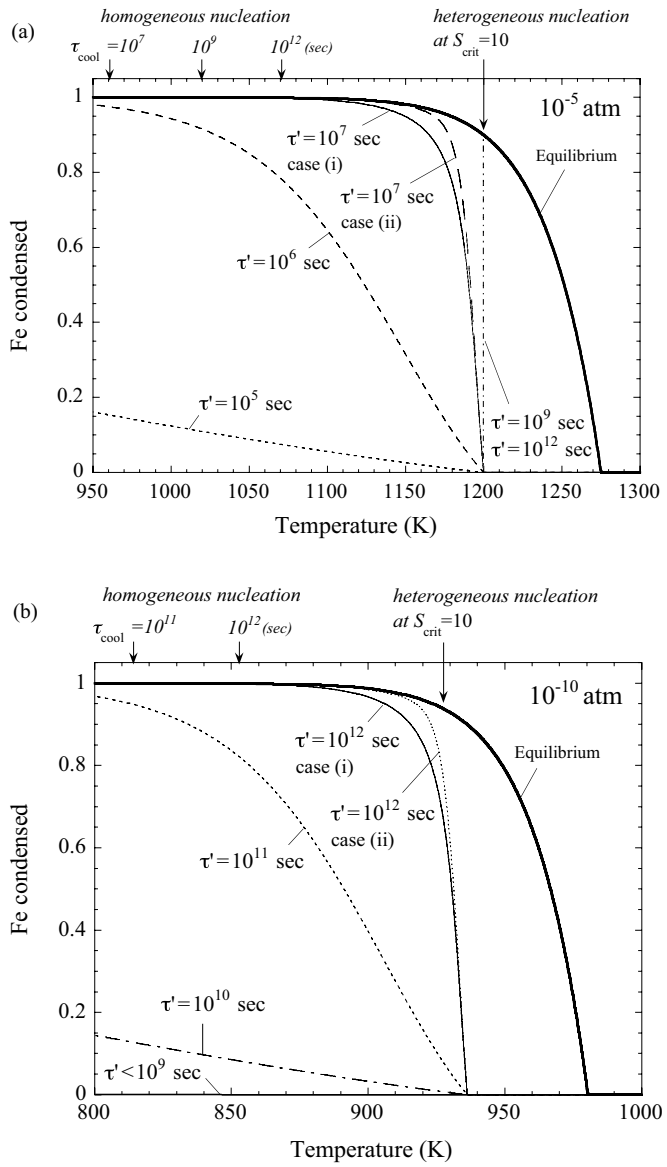

Figure 7. Change in the condensed fraction of iron in the system cooled at different timescales, $\tau' = \tau_{cool}/(d_{cor}/1\,\mu m)$, is shown as a function of temperature (see the text for detail). Heterogeneous nucleation of metallic iron was assumed to occur on pre-existing corundum grains at $S = 10$. Homogeneous nucleation temperatures for metallic iron for $\tau_{cool} = 10^7$–10^{12} s are indicated as arrows (Kozasa & Hasegawa 1987). The equilibrium condensation curve is also shown as a reference (thick solid curve). Condensation behaviors with different sets of α_c were calculated (cases (1) and (2); see the text for detail), but both results are shown only when they differed. The total pressure of the system was set to (a) 10^{-5} atm and (b) 10^{-10} atm.

All iron atoms condense through heterogeneous nucleation and growth in cases where τ' is $>10^7$ s. In the case of $\tau' = 10^5$ s, which corresponds to the formation timescale of chondrules, homogeneous nucleation may take place because most of the gas remains as vapor at low temperatures due to rapid cooling and these low temperatures (and high values of S) would drive homogeneous nucleation.

The effect of α_c (cases (1) and (2)) is not significant for condensation in the case of slow cooling (e.g., $\tau' = 10^9$ and 10^{12} s), which are the timescales for vertical movement of disk materials and for radial movement of disk materials if $d_{cor} = 1\,\mu m$. This is because the cooling timescale is much longer than the reaction timescales for both cases (1) and (2). No difference between cases (1) and (2) was found in the case of rapid cooling ($\tau' = 10^5$ and 10^6 s) as well because condensation occurs under highly non-equilibrium conditions (keeping $S > 10$ with α_c of unity in both cases). The difference in α_c in cases (1) and (2) was seen for condensation in a system cooled with the intermediate timescale of $\tau' = 10^7$ s, similar to the cooling timescale of igneous refractory inclusions in chondrites if $d_{cor} = 1\,\mu m$ (Stolper & Paque 1986). Condensation proceeds more slowly in case (1) due to kinetic hindrances (smaller α_c) for $1 < S < 10$.

The condensation behavior at a total pressure of 10^{-10} atm is shown in Figure 7(b). The cooling timescale of outflows from evolved stars is likely to be $\tau_{cool} < 10^{10}$ s (e.g., Sogawa & Kozasa 1999; Gail 2003), and heterogeneous nucleation and growth of metallic iron may not occur effectively on 1 μm sized pre-existing corundum grains due to kinetic reasons (curves for $\tau' < 10^{10}$ s in Figure 7(b)). It should be noted, however, that the condensation of metallic iron via heterogeneous nucleation on corundum grains may occur if $d_{cor} < 0.1\,\mu m$ ($\tau' > 10^{11}$ s).

Although more experimental data on condensation of metallic iron under various condensation conditions and on homogeneous nucleation of nucleation seeds (corundum in the present case) are needed, we conclude that the formation of metallic iron does not take place at equilibrium in outflows from evolved stars and for thermal events with timescales of $<10^7$ s in the protoplanetary disks.

6. CONCLUSIONS

Evaporation and condensation experiments using metallic iron under known undersaturation and supersaturation ratios show that (1) metallic iron condenses at the maximum rate ($\alpha_c = 1$) under high supersaturation conditions ($S > 10$) and evaporates nearly ideally ($\alpha_e = 1$) at $S \sim 0$, (2) evaporation of metallic iron takes place with kinetic hindrance at S close to 1, and (3) metallic iron nucleates heterogeneously on an Al_2O_3 substrate at $S > 10$. Metallic iron does not necessarily condense homogeneously in circumstellar environments as discussed in previous studies, but can condense through heterogeneous nucleation on pre-existing dust with a smaller degree of supercooling. Metallic iron formation proceeds with little kinetic hindrance for highly supersaturated or undersaturated conditions, but kinetic effects such as surface atomistic processes should be considered for evaporation and condensation occurring with S close to unity.

We thank Joseph A. Nuth III for comments and suggestions, which helped us to improve the manuscript. This work was supported by Grant-in-Aid for Young Scientists (A) (20684025).

REFERENCES

Anders, E., & Grevesse, N. 1989, Geochim. Cosmochim. Acta, 53, 197
Blander, M., & Katz, J. L. 1967, Geochim. Cosmochim. Acta, 31, 1025
Choi, B.-G., Huss, G. R., Wasserburg, G. J., & Gallino, R. 1998, Science, 282, 1284
Dayton, B. B. 1956, in National Symposium on Vacuum Technology Transactions, Gas Flow Patterns at Entrance and Exit of Cylindrical Tubes, ed. E. S. Perry & J. H. Durant (London: Pergamon), 5
Gail, H.-P. 2003, in Astromineralogy, ed. T. K. Henning (Berlin: Springer), 55
Kemper, F., de Koter, A., Waters, L. B. F. M., Bouwman, J., & Tielens, A. G. G. M. 2002, A&A, 384, 585
Kozasa, T., & Hasegawa, H. 1987, Prog. Theor. Phys., 77, 1402
Nittler, L. R., Alexander, C. M. O'D., Gao, X., Walker, R. M., & Zinner, E. 1997, ApJ, 483, 475

Ozawa, K., & Nagahara, H. 2000, Geochim. Cosmochim. Acta, 64, 939
Paule, R. C., & Margrave, J. L. 1967, in The Characterization of High-Temperature Vapors, ed. J. L. Margrave (New York: Wiley), 130
Sata, T., Sasamoto, T., & Lee, H.-L. 1978, Rep. Res. Lab. Eng. Mater. Tokyo Inst. Technol., 3, 41
Sogawa, H., & Kozasa, T. 1999, ApJ, 516, L33
Stolper, E., & Paque, J. M. 1986, Geochim. Cosmochim. Acta, 50, 1785
Tachibana, S., Tsuchiyama, A., & Nagahara, H. 2002, Geochim. Cosmochim. Acta, 66, 713
Takigawa, A., Tachibana, S., Nagahara, H., Ozawa, K., & Yokoyama, M. 2009, ApJ, 707, L97
Takigawa, A., Tachibana, S., Nagashima, K., Makide, K., Huss, G. R., Krot, A. N., Nagahara, H., & Ozawa, K. 2011, Lunar Planet Sci., 42, 2599
Tsuchiyama, A., & Fujimoto, S. 1995, in Proc. NIPR Symp. 8, Antarctic Meteorites, ed. K. Yanai (Tokyo: NIPR), 205